

DOI: 10.1002/ ((please add manuscript number))

Article type: (Full Paper)

Honeycomb-like spherical cathode host constructed from hollow metallic and polar Co₉S₈ tubules for advanced lithium-sulfur batteries

*Chunlong Dai, Jin-Myoung Lim, Minqiang Wang, Linyu Hu, Yuming Chen, * Zhaoyang Chen, Hao Chen, Shujuan Bao, Bolet Shen, Yi Li, Graeme Henkelman, * Maowen Xu**

C. L. Dai, M. Q. Wang, L. Y. Hu, Z. Y. Chen, H. Chen, Prof. S. J. Bao, B. L. Shen, Y. Li, Prof. M. W. Xu

Faculty of Materials and Energy, Southwest University, Chongqing 400715, P.R. China.

E-mail: xumaowen@swu.edu.cn

Dr. J. M. Lim and Prof. G. Henkelman

Texas Materials Institute and Department of Chemistry and the Institute for Computational Engineering and Sciences, University of Texas at Austin, Austin, Texas 78712, United State.

E-mail: henkelman@utexas.edu

Dr. Y. M. Chen

Department of Nuclear Science and Engineering, Department of Materials Science and Engineering, Massachusetts Institute of Technology, Cambridge, Massachusetts 02139, USA.

E-mail: yumingc@mit.edu

This is the author manuscript accepted for publication and has undergone full peer review but has not been through the copyediting, typesetting, pagination and proofreading process, which may lead to differences between this version and the [Version of Record](#). Please cite this article as [doi: 10.1002/adfm.201704443](https://doi.org/10.1002/adfm.201704443).

This article is protected by copyright. All rights reserved.

Keywords: hollow Co_9S_8 tubules, honeycomb-like sphere, lithium sulfur batteries, lithium polysulfides, reaction kinetics

Lithium-sulfur (Li-S) batteries have been investigated as promising next-generation electrical energy storage systems in view of their high energy density and low cost. The practical application of this battery, however, remains remote because of rapid capacity fade caused by the low conductivity of sulfur, dissolution of intermediate lithium polysulfides, severe volumetric expansion, and slow redox kinetics of polysulfide intermediates. Here, to address these obstacles, we design a new sulfiphilic and highly conductive honeycomb-like spherical cathode host constructed from hollow metallic and polar Co_9S_8 tubes. Co_9S_8 can effectively bind polar polysulfides for prolonged cycle life, due to the strong chemisorptive capability for immobilizing the polysulfide species. The hollow structure, as the sulfur host, can further prevent polysulfide dissolution and offer sufficient space to accommodate the necessary volume expansion. Well-aligned tubular arrays provide a conduit for rapid conduction of electrons and Li-ions. More importantly, the experimental results and theoretical calculations show that Co_9S_8 plays an important catalytic role in improving the electrochemical reaction kinetics. When used as cathode materials for Li-S batteries, the $\text{S}@\text{Co}_9\text{S}_8$ composite cathode exhibits high capacity and an exceptional stable cycling life demonstrated by tests of 600 cycles at 1 C with a very low capacity decay rate of only $\sim 0.026\%$ per cycle.

1. Introduction

Traditional lithium-ion batteries (LIBs) based on intercalation reactions are not expected to satisfy the ever-growing demands of large-scale energy storage systems and electric vehicles due to their limited theoretical energy density and high price.^[1-3] Lithium-sulfur (Li-S) batteries, based on multielectron redox conversion, are regarded as one of the most promising alternatives for LIBs in

view of their high theoretical specific capacity (1672 mA h g^{-1}) and energy density (2600 W h kg^{-1}).^[4-6]

Furthermore, advantages such as the natural abundance, low cost, and nontoxicity should help Li-S batteries become commercially competitive as compared to current LIBs.^[7] However, Li-S batteries remain absent from practical applications due to several significant limitations. First, the poor conductivity of sulfur and lithium sulfides leads to a low utilization of the active material. Second, the severe volumetric expansion ($\sim 80\%$) during cycling results in rapid destruction of the electrode. Third, the dissolution of intermediate lithium polysulfides (LiPSs) into the electrolyte and the shuttle effect between the electrodes give rise to poor cycling stability and low Coulombic efficiency.^[8-9] In addition, the slow redox kinetics associated with polysulfide intermediates is a serious issue.^[10-13]

Many strategies have been developed to overcome these challenges and to improve the electrochemical performance of Li-S batteries. One effective strategy is to use carbon materials with designed pore structures as encapsulation hosts for sulfur, including as porous graphene,^[14,15] carbon spheres,^[16,17] carbon nanotubes^[18,19] and nanofibers.^[20] These carbonaceous materials can accelerate the electron transfer of the electrode, but are not able to suppress polysulfide shuttling due to a weak chemical interaction between nonpolar carbons and the polar LiPSs (**Figure 1a**). The dissolved intermediate LiPSs deposit on the carbon hosts and the anode, thus reducing cycling stability.

Recently, polar materials, such as TiO_2 ,^[21,22] MnO_2 ,^[23-25] SiO_2 ,^[26, 27] and $\alpha\text{-Ni(OH)}_2$,^[28,29] have been demonstrated to strongly bind LiPSs and efficiently constrain LiPSs to the cathode and thus achieve cycling stability. However, most of these metal oxides and metal hydroxides are semiconductors, which could hinder electron transport and lead to inferior rate capabilities. An appropriate sulfur host should possess both strong polysulfide affinity and excellent conductivity.^[30-32] Furthermore,

the solid structure of these materials is only able to fix a small amount of LiPSs on their surface because the interaction between polar materials and LiPSs is based on monolayer chemical adsorption.^[5,33-35] The LiPSs far from the surface can still dissolve into the electrolyte and shuttle between the electrodes (Figure 1b). A promising design is to construct polar hollow tubules that can also physically block the outward diffusion pathways and thus encapsulate LiPSs in the internal void space at the cathode (Figure 1c). Therefore, hollow nanotubes can offer more efficient confinement of LiPSs than other forms, such as particles and sheets.

In addition to the aforementioned strategies, employing catalysts to enhance LiPSs redox is another innovative way to suppress diffusion of LiPSs.^[36-38] The electrochemical discharge/charge processes are kinetically sluggish due to the insulating nature of sulfur and LiPSs. For these non-catalytic hosts, the conversion reaction of LiPSs is slow and the intermediate lithium polysulfides can easily diffuse into the electrolyte (Figure 1d). However, soluble long-chain LiPSs can be efficiently converted to solid phases of sulfur and $\text{Li}_2\text{S}_2/\text{Li}_2\text{S}$ due to the accelerated polysulfide redox kinetics when used as catalytic hosts (Figure 1e). Therefore, the application of catalytic materials as a sulfur host is a promising strategy to build advanced Li-S batteries.

Here we have designed and prepared highly conductive sulfiphilic honeycomb-like spheres constructed from hollow, metallic, and polar Co_9S_8 tubules as the sulfur host. This cathode host enables a highly stable sulfur electrode for the following reasons. First, Co_9S_8 has polar chemisorptive capability for fixing the LiPSs and ensures fast charge migration during cycling due to its metallic nature.^[39] Second, the one-dimensional tubular structure, with a high aspect ratio, acts as a conduit to accelerate the transport of electrons and ions, which is superior than isolated nanoparticles. Moreover, the elaborate structure of the aligned tubules is able to form a better

conductive framework at the nanoscale when compared to their random counterparts.^[40] Third, the shell of nanotube acts as a gate to encapsulate the LiPSs in the internal void space. Therefore, these Co_9S_8 tubules prevent the loss of LiPSs via structural and chemical dual-encapsulation. In addition, the hollow tubular structure possesses large internal void space which effectively relieves the volumetric expansion of sulfur during cycling and provides the space to load a relatively high content of sulfur. More importantly, Co_9S_8 plays an important catalytic role in improving the electrochemical reaction kinetics. As a result, when used as a sulfur host for Li-S batteries, the synthesized composite enables high capacities and maintains a stable cycling performance.

2. Results and Discussion

The synthesis of the $\text{S}@\text{Co}_9\text{S}_8$ composites is illustrated in **Figure 2a**. In the first step, the precursor, with an urchin-like structure constructed from nanorods, has been prepared *via* a facile chemical process. Afterwards, we transform the nanorods into hollow structures of Co_9S_8 through a sulfidation reaction. Finally, sulfur is steamed into the Co_9S_8 nanotubes by a melting-diffusion process.

Figure S1a and b show the FESEM and TEM image of the as-prepared precursor. It can be seen that the precursor displays an urchin-like morphology consisting of nanorods. The diameter of the urchin and the nanorod structures are estimated to be about 10 μm and 100 nm, respectively. The corresponding XRD pattern (Figure S2) confirms that the precursor is consistent with the $\text{Co}(\text{CO}_3)_{0.5}\text{OH}\cdot 0.11\text{H}_2\text{O}$ phase. The solid nanorod can be turned into a hollow tubular structure by an anion exchange reaction (Figure 2b-d).^[41-43] The hollow tubular structure offers more active sites for electrochemical reactions as compared to their solid counterparts. As shown in Figure 2e, the XRD pattern of the product after sulfidation shows that the diffraction peaks are perfectly assigned to

Co₉S₈ (JCPDS No.86-2273). It is worth mentioning that the product still possesses the sphere-like morphology after sulfidation (Figure 2b). The morphology of the honeycomb-like spheres composed of hollow tubules provides a faster conduction pathway for electron and Li ion as compared with isolated nanoparticles and random tubules. Furthermore, the hollow Co₉S₈ tubules have an ultrahigh aspect ratio (Figure S3), which provides fast electron and Li ion migration during cycling. The composite structure was further characterized by energy-dispersive X-ray spectroscopy (EDS) mapping (Figure S4) revealing a homogeneous dispersion of Co and S throughout the samples; no other elements were observed (Figure S5). TEM images show the tubules with an internal diameter of 50 nm (Figure 2d), which is consistent with FESEM observations. HRTEM study shows a clear lattice spacing of 0.3 nm, corresponding to the (311) plane of Co₉S₈ (Figure 2d).^[44,45] The selected area electron diffraction of Co₉S₈ suggests the obtained sample is polycrystalline substance (Figure S6). The nitrogen sorption measurement shows a specific surface area of 43 m² g⁻¹ and the existence of pores with diameters below 10 nm (Figure S7).

Sulfur can infiltrate into hollow Co₉S₈ tubules using the melt-diffusion method. Figure 2i shows the XRD pattern of the composite after sulfur loading at 155 °C, indicating highly crystalline cubic sulfur (JCPDS No. 08-0247) and Co₉S₈ (JCPDS No.86-2273). TGA was used to determine that the content of sulfur in the composite was as high as 70 wt% (see Figure S8). The S@Co₉S₈ composite maintains a spherical structure (Figure 2f and g). No sulfur is observed on the outer surface of the Co₉S₈ tubules (Figure 2g and h), indicating efficient sulfur removal when the tubules are immersed in a CS₂ and ethanol mixture. The boundaries between the cavity and the shell become blurry, indicating the successful diffusion of sulfur into the tubule. More importantly, no large sulfur particles were recorded. EDX mapping (Figure S9) showed a homogeneous distribution of Co and S in the cavity of

Co₉S₈ tubules. The EDS spectrum of the S@Co₉S₈ composite (Figure S10) shows that the S intensity is much higher than that of pure Co₉S₈, indicating an increase of sulfur in the Co₉S₈ tubules.

Here we used a combination of visual discrimination, XPS analysis and first-principles surface calculations to investigate the interaction between Co₉S₈ tubules and LiPSs. The synthesized LiPSs are dissolved in dimethoxymethane (DME) to form a yellow solution. As displayed in **Figure 3a**, the color of the solution is maintained after the addition of carbon. However, the yellow solution turns colorless after several hours with the addition of Co₉S₈ (Figure 3b), demonstrating the strong adsorption capability of the polar Co₉S₈. XPS was used to investigate the difference of the chemical state of Co between pristine Co₉S₈ and Co₉S₈+Li₂S₄. As displayed in Figure 3c, the Co 2p_{3/2} XPS spectrum of pristine Co₉S₈ tubules can be described by a spin-orbit doublet and a shake-up satellite. The peaks of the spin-orbit doublet, located at ~781.1 and ~778.5 eV, are consistent with literatures values for Co₉S₈.^[46] After contact with Li₂S₄, the peaks shift to ~778.9 and ~777.6 eV (Figure 3d). The variation of the peak positions can be attributed to electron transfer from Li₂S₄ to the Co atoms, indicating a strong chemical interaction between Co₉S₈ and the LiPSs.^[34,47] To further understand the mechanism of the visual discrimination (Figure 3b) and XPS results (Figure 3d), we performed first-principles calculations of the binding energies of intermediate LiPSs (Li₂S₄, Li₂S₆, and Li₂S₈) on both the (311) and (440) surfaces of Co₉S₈, as shown in Figure 3e and f. Figure 3e shows atomic structures of Li₂S₄ adsorbed on the (311) and (440) surfaces of Co₉S₈, showing that Li can make bonds with S on the Co₉S₈ surfaces, and that S can also make bonds with Co on Co₉S₈ surfaces because of Coulomb interactions between the cations and anions. Based on the formations of the bonds, these three LiPSs are likely to be adsorbed on the both Co₉S₈ surfaces based upon the positive binding energies

in each case (Figure 3f). Interestingly, binding energies on the (311) surface have larger values than those on the (440) surface, suggesting that the (311) surface more effectively captures LiPSs.

A combination of cyclic voltammetry (CV), galvanostatic discharge-charge tests and DFT calculations were used to investigate the catalytic effect of Co_9S_8 on LiPS redox reactions. **Figure 4a** shows the CV profiles of pure S and $\text{Co}_9\text{S}_8+\text{S}$ electrodes at a scan rate of 0.1 mV s^{-1} . The CV curves of the pure sulfur and $\text{Co}_9\text{S}_8+\text{S}$ electrode both display two cathodic peaks and one anodic peak. Compared to a pure sulfur electrode, the peaks of $\text{S}@\text{Co}_9\text{S}_8$ electrodes are sharper with a higher intensity. Figure S11a shows a comparison of the peak potentials of the two electrodes for the redox reactions. For the pure sulfur electrode, two deformed and widened cathodic peaks are located at 2.21 and 1.98 V and the anodic peak is at 2.44 V. Two sharp cathodic peaks located at 2.26 and 2.04 V and the anodic peak located at 2.38 V for the $\text{Co}_9\text{S}_8+\text{S}$ electrode are also seen. Both cathodic peaks for $\text{Co}_9\text{S}_8+\text{S}$ have a positive shift and the anodic peak has a negatively shift, indicating that Co_9S_8 can significantly suppress the electrochemical polarization. This finding can be attributed to the catalytic effect of Co_9S_8 on the oxidation/reduction of $\text{Li}_2\text{S}/\text{S}$.^[48-50] A comparison of onset potentials is also studied to further analyze the effect of Co_9S_8 . The onset potential of the $\text{Co}_9\text{S}_8+\text{S}$ electrode (Figure S11b) in the oxidation reaction is 2.14 V, which is different from that of pure sulfur (2.33 V). For the reduction reaction, the onset potentials for $\text{Co}_9\text{S}_8+\text{S}$ are 2.37 and 2.11 V, compared with 2.32 and 2.08 V for the pure sulfur electrode. It is clear that the $\text{Co}_9\text{S}_8+\text{S}$ electrode shows a higher onset reduction potential and a lower onset oxidation potential than pure sulfur. Figure 4b shows discharge/charge voltage profiles of pure S and the $\text{Co}_9\text{S}_8+\text{S}$ electrode at 0.2 C. The $\text{Co}_9\text{S}_8+\text{S}$ electrode has a discharge capacity of 847 mAh g^{-1} and a reversible charge capacity of 856 mAh g^{-1} , both much larger than that of the pure sulfur electrode. Moreover, the $\text{Co}_9\text{S}_8+\text{S}$ electrode possesses a relatively

low polarization value of 225 mV between the charge and discharge plateaus, which is much lower than that of 310 mV for the pure sulfur electrode.^[51] The improved discharge capacity and reductive polarization show that Co₉S₈ is able to boost the electrochemical reaction kinetics during the discharge/charge processes in Li-S batteries.

To elucidate details of the chemisorptive capability of LiPSs on the Co₉S₈ surfaces, we used the CINEB method with DFT to calculate the dissociation barriers between Li and S of LiPSs on both the (311) and (440) Co₉S₈ surfaces ($\text{Li}_2\text{S}_x \rightarrow \text{LiS}_x + \text{Li}^+ + \text{e}^-$). From these calculations, we determine the decomposition mechanism as the Li ion moves far away from the S ions in LiPSs. Previous studies reported that the chemical interaction between Li ions and graphene is weak and the dissociation barrier is very high (around 1.81 eV).^[48] As shown in Figure 4c and d, the height of all the dissociation barriers for Li₂S₄, Li₂S₆, and Li₂S₈ on both (311) and (440) surfaces of Co₉S₈ are lower than 0.6 eV, demonstrating that the decomposition reaction kinetics of LiPSs on Co₉S₈ surfaces is more facile than on graphene. For this enhanced catalytic activity of Co₉S₈, delithiation reaction kinetics of Co₉S₈ in the electrochemical profiles can be facilitated as shown in Figure 4a and b. These results show that the transformation efficiency of soluble LiPSs to final insoluble products is enhanced, which substantially decreases LiPSs shuttling into the electrolyte.^[52] Figure 4e and 4f show the process of Li-S dissociation into relaxed structures for Li₂S₄ on (311) and (440) surfaces of Co₉S₈, respectively.

We next evaluated the electrochemical performance of the S@Co₉S₈ nanocomposite as a cathode material for Li-S batteries. **Figure 5a** shows the rate capabilities of the S@Co₉S₈ composite at various current densities from 0.2 to 2 C. Benefitting from the high conductivity and fast reaction kinetics, the S@Co₉S₈ cathode delivers reversible capacities of ~1136, ~1011, ~893, ~842, and ~806 mAh g⁻¹ at 0.2, 0.5, 1, 1.5, and 2 C, respectively. After high-rate cycling, when the current density returns to 0.2

C, a reversible capacity of 1093 mAh g⁻¹ is recovered, indicating excellent stability of the S@Co₉S₈ composite structure. Figure 5b shows the charge/discharge voltage profiles at various current rates. The small potential differences between the charge/discharge voltage plateaus at various current densities and long second-discharge plateau confirm that the S@Co₉S₈ electrode possesses small polarization and fast reaction kinetics, which is consistent with the CV result (Figure S12). Figure 5c shows the long-term cycling performance of the S@Co₉S₈ composite electrodes at a current density of 1 C. A discharge capacity of 893.7 mAh g⁻¹ is obtained in first cycle, and more importantly, a capacity of 756.6 mAh g⁻¹ is maintained after 600 cycles, with a low decay rate of 0.026% per cycle. The excellent stability of the S@Co₉S₈ cathode can be due to polar Co₉S₈ that can fix LiPSs by strong chemical action and the unique hollow structure that can physically block the outward diffusion pathways. Moreover, high Coulombic efficiency above 98.5% is maintained throughout long-term cycling, which further indicates that the Co₉S₈ host effectively prevents the dissolution of polysulfide to the electrolyte. The outstanding stability and high Coulombic efficiency show that the LiPSs are not able to poison the Co₉S₈ during cycling. S@carbon black (S@CB) composite was prepared as a comparison (Figure S13). The S@CB electrode delivers low Coulombic efficiency and rapid capacity decay (Figure S14). The Coulombic efficiency is only 92.2% after 100 cycles and the rate of capacity decay is 0.41% per cycle. It is worth mentioning that pure Co₉S₈ does not contribute to capacity under the same conditions (Figure S15). The corresponding discharge-charge curve is displayed in Figure S14.

To explore the relationship between the structure and electrochemical properties, we performed a postmortem study by FESEM. As shown in Figure 5d and e, the honeycomb-like morphology of the S@Co₉S₈ composite is retained after cycling, indicating that the internal void space of Co₉S₈

nanotube offers sufficient room to accommodate the volume expansion of sulfur during the lithiation process. The separators of the S@Co₉S₈ and S@CB electrodes after 600 cycles at 1 C are also studied (Figure S16). The separator for the S@Co₉S₈ electrode shows less color than the S@CB electrode, confirming that the polar Co₉S₈ effectively restricts LiPSs dissolution into the electrolyte. To the best of our knowledge, the decay rate per cycle of the S@Co₉S₈ electrode is much lower than that of other cobalt sulfide@S composites. Furthermore, there is no trace of LiPSs after cycling in Figure 5d and 5e, which means that although Co₉S₈ has higher binding energies with LiPSs (Figure 3f), LiPSs would not fully poison Co₉S₈ after cycling due to the superior catalytic activity (Figure 4d and 4e). This point also can be brought up by stable electrochemical profiles after 2nd, 5th, 10th, and 20th cycles (Figure S18a) and retained Co₉S₈ after cycling (Figure S18b).

3. Conclusion

In summary, we have fabricated uniform honeycomb-like spheres constructed from hollow metallic and polar Co₉S₈ tubules as a hollow sulfur host for Li-S batteries. The honeycomb-like spheres enhance conduction of electrons and Li ions and inhibit LiPS diffusion. Experiment and simulation show that Co₉S₈ is a polysulfide immobilizer and electrocatalyst in Li-S batteries. Benefiting from excellent conductivity, strong LiPSs adsorption capability, and high catalytic activity, the S@Co₉S₈ composite cathode delivers a stable cycle life with a high discharge capacity for Li-S batteries.

4. Experimental Section

Synthesis of honeycomb-like spheres constructed from hollow, metallic, and polar

Co₉S₈ tubules: In a typical synthesis, 1 mmol of Co(NO₃)₂·6H₂O, 2.5 mmol of NH₄F, and 5 mmol of urea were dissolved in 20 ml of deionized water. The solution was

transferred into a 40 ml Teflon-lined autoclave and kept at 120 °C for 6 h. After cooling down to room temperature, the pink precursor was taken out and washed several times with deionized water. Then, the as-prepared precursor and 0.96 g $\text{Na}_2\text{S}\cdot 9\text{H}_2\text{O}$ were added into 20 ml water under magnetic stirring. The solution was transferred into a 40 ml Teflon-lined autoclave and maintained in an oven at 120 °C for 6 h. Finally, the black Co_9S_8 was collected by filtration, washed with deionized water, and dried overnight at 60 °C under vacuum.

Synthesis of S@Co₉S₈: The as-prepared Co_9S_8 nanotubes and sublimed sulfur (1:4, weigh ratio) were well mixed and heated at 155 °C for 12 h in a tube furnace under an Ar atmosphere. In order to remove the excrescent sulfur outside the Co_9S_8 nanotubes, the product was immersed in a 10 ml CS_2 and ethanol solution (1:4, volume ratio) at room temperature for 10 min.

Synthesis of S@CB: The carbon black (CB) and sublimed sulfur (3:7, weigh ratio) were well mixed and heated at 155 °C for 12 h in a tube furnace under an Ar atmosphere.

Fabrication of the Co₉S₈+S and pure S electrode: The Co_9S_8 +S electrode was synthesized by simply mixing sulfur, Co_9S_8 , CB, and polyvinylidene fluoride (PVDF) binder with a weight ratio of 60:20:10:10. The pure S electrode was prepared by simply mixing sulfur, CB, and PVDF binder with a weight ratio of 60: 20: 20.

Materials characterization: The morphology and microstructure were examined by field emission scanning electron microscopy (FESEM, JSM-6700F, Japan), energy dispersive spectroscopy (EDS, JEOL-6300F) and transmission electron microscopy (TEM, JEM-2100, Japan). The crystal structures

were characterized by powder X-ray diffraction (XRD, MAXima-X XRD-7000) with Cu K α radiation ($\lambda = 1.5406$ nm). Thermogravimetric analysis (TGA, Q50, USA) was performed to estimate the content of S in the prepared composite. The specific surface area and analysis of the pore size distribution of products were performed by Brunauer-Emmett-Teller (BET) method (Quantachrome Instruments, USA). X-ray photoelectron spectroscopy (XPS) measurements were conducted by Thermo Scientific ESCALAB 250Xi electron spectrometer.

Electrochemical measurements: The working electrode was prepared by a slurry coating procedure. The electrodes were fabricated by mixing active materials (S@Co₉S₈), Super-P carbon black, and PVDF binder with a weight ratio of 75:15:10 in N-Methyl-2-pyrrolidone (NMP). The slurry was then uniformly deposited onto a clean and polished aluminum current collector. Finally, the electrodes were dried under vacuum at 60 °C for 12 h to remove the NMP solvent. CR3025 coin cells were assembled in an argon-filled glove box. Li foil was used as the counter electrode. The electrolyte was 1 M bis(trifluoromethane) sulfonimide lithium salt (LiTFSI) dissolved in a mixture of 1,3-dioxolane (DOL) and dimethoxymethane (DME) (volume ratio of 1:1) with 0.1 M LiNO₃ as the electrolyte additive. All cells were aged for several hours before cycling to ensure an adequate penetration of the electrolyte into the electrode. The coin cells were galvanostatically cycled at different current densities between 1.7 and 2.8 V (vs. Li/Li⁺) on a Land cycler (Wuhan Kingnuo Electronic Co., China). The cyclic voltammetry (CV) test was recorded on a CHI 660c electrochemical workstation (Shanghai Chenhua, China) at a scanning rate of ~ 0.1 mV s⁻¹. The specific capacities were calculated based on the sulfur mass.

Density functional theory surface calculations: To provide a fundamental understanding of LiPSs capture in Co₉S₈, we have carried out DFT calculations of the

interaction and dissociation of LiPSs on the (311) and (440) surfaces of Co_9S_8 . The Vienna Ab-initio Simulation Package was used to perform spin-polarized DFT calculations,^[53] with a plane-wave basis set and the projector augmented-wave method.^[54] A generalized gradient approximation functional, parameterized by Perdew-Burke-Ernzerhof, was used to described electronic exchange and correlation.^[55] The cut-off energy and k-point meshes for each structures were determined by energy convergence tests to within 0.2 meV/atom. All bulk calculations, providing the basis of our surface models, were performed using fully relaxed structures; the surface calculations were conducted at fixed volume. For the bulk atomic model, cubic Co_9S_8 (Space group: $Fd-3m$, $a=9.8045 \text{ \AA}$) consisting of 36 Co and 32 S atoms was used as shown in Figure S19a. LiPSs (Li_2S_4 , Li_2S_6 , and Li_2S_8) were used as represented in Figure S19b-d. Stoichiometric (311) and (440) surface models for Co_9S_8 were developed using 136 and 68 atoms, respectively, with a vacuum layer ($>10 \text{ \AA}$) on the cleaved (311) and (440) surfaces as described in Figure S19e and 19f. The climbing image nudged elastic band (CINEB) method was used to calculate dissociation energy barriers.^[56,57] Van der Waals interactions between the Co_9S_8 surface and the LiPSs were included using the vdW-DF2 functional.^[58] Finally, binding energies E_b between LiPSs and Co_9S_8 surfaces were calculated as

$$E_b = E_{\text{LiPS}_S} + E_{\text{Co}_9\text{S}_8} - E_{\text{LiPS}_S+\text{Co}_9\text{S}_8}$$

Supporting Information

Supporting Information is available from the Wiley Online Library or from the author.

Acknowledgements

This work is financially supported by grants from the National Natural Science Foundation of China (No. 21773188), Basic and frontier research project of Chongqing (cstc2015jcyjA50031) and Fundamental Research Funds for the Central Universities (XDJK2017D004, XDJK2017A002, XDJK2017B048) and program for Innovation Team Building at Institutions of Higher Education in Chongqing (CXTDX201601011) and the Welch Foundation (F-1841). Computational resources were provided by the Texas Advanced Computing Center.

Received: ((will be filled in by the editorial staff))

Revised: ((will be filled in by the editorial staff))

Published online: ((will be filled in by the editorial staff))

References

- [1] Z. Cui, C. Zu, W. Zhou, A. Manthiram, J.B. Goodenough, *Adv. Mater.* **2016**, 28, 6926.
- [2] Z.W. Seh, Y. Sun, Q. Zhang, Y. Cui, *Chem. Soc. Rev.* **2016**, 45, 5605.
- [3] Q. Pang, X. Liang, C. Y. Kwok, L.F. Nazar, *Nat. Energy.* **2016**, 1, 16132.
- [4] R. Fang, S. Zhao, Z. Sun, D. W. Wang, H. M. Cheng, F. Li, *Adv. Mater.* **2017**, 1606823.
- [5] Z. Li, H. B. Wu, X. W. Lou, *Energy Environ. Sci.* **2016**, 9, 3061.
- [6] X. Liu, J. Q. Huang, Q. Zhang, L. Mai, *Adv. Mater.* **2017**, 1601759.
- [7] S. Rehman, K. Khan, Y. Zhao, Y. Hou, *J. Mater. Chem. A* **2017**, 5, 3014.
- [8] B. C. Yu, J. W. Jung, K. Park, J. B. Goodenough, *Energy Environ. Sci.* **2017**, 10, 86.

This article is protected by copyright. All rights reserved.

- [9] H. J. Peng, J. Q. Huang, X. Y. Liu, X. B. Cheng, W. T. Xu, C. Z. Zhao, F. Wei, Q. Zhang, *J. Am. Chem. Soc.* **2017**, DOI: 10.1021/jacs.6b12358.
- [10] Z. Yuan, H. J. Peng, T. Z. Hou, J. Q. Huang, C. M. Chen, D. W. Wang, X. B. Cheng, F. Wei, Q. Zhang, *Nano Lett.* **2016**, *16*, 519.
- [11] Z. Chang, H. Dou, B. Ding, J. Wang, Y. Wang, X. Hao and D. R. MacFarlane, *J. Mater. Chem. A* **2017**, *5*, 250.
- [12] G. Babu, K. Ababtain, K. Y. S. Ng and L. M. R. Arava, *Sci. Rep.* **2015**, *5*, 8763.
- [13] X. Tao, J. Wang, C. Liu, H. Wang, H. Yao, G. Zheng, Z. W. Seh, Q. Cai, W. Li, G. Zhou, C. Zu and Y. Cui, *Nat. Commun.* **2016**, *7*, 11203.
- [14] J. Song, Z. Yu, M. L. Gordin and D. Wang, *Nano Lett.* **2016**, *16*, 864-870.
- [15] P. Y. Zhai, H. J. Peng, X. B. Cheng, L. Zhu, J. Q. Huang, W. C. Zhu, Q. Zhang, *Energy Storage Mater.* **2017**, *7*, 56.
- [16] Z. Zhang, G. Wang, Y. Lai, J. Li, Z. Zhang, W. Chen, *J. Power Sources* **2015**, *300*, 157.
- [17] Y. J. Zhong, S. F. Wang, Y. J. Sha, M. L. Liu, R. Cai, L. Li, Z. P. Shao, *J. Mater. Chem. A* **2016**, *4*, 9526.
- [18] R. Fang, S. Zhao, P. Hou, M. Cheng, S. Wang, H. M. Cheng, C. Liu, F. Li, *Adv. Mater.* **2016**, *28*, 3374.
- [19] K. Mi, Y. Jiang, J. Feng, Y. Qian and S. Xiong, *Adv. Funct. Mater.* **2016**, *26*, 1571.
- [20] S. Lu, Y. Cheng, X. Wu, J. Liu, *Nano Lett.* **2013**, *13*, 2485.

- [21] Z.W. Seh, W.Y. Li, J.J. Cha, G.Y. Zheng, Y. Yang, M.T. McDowell, P.C. Hsu, Y. Cui, *Nat. Commun.* **2013**, *4*, 1331.
- [22] Z. Xiao, Z. Yang, L. Wang, H. Nie, M. Zhong, Q. Lai, X. Xu, L. Zhang, S. Huang, *Adv. Mater.* **2015**, *27*, 2891.
- [23] X. Wang, G. Li, J. Li, Y. Zhang, A. Wook, A. Yu Z. Chen, *Energy Environ. Sci.* **2016**, *9*, 2533.
- [24] Z. Li, J. Zhang, X. W. Lou, *Angew. Chem. Int. Ed.* **2015**, *54*, 12886.
- [25] X. Liang, C. Hart, Q. Pang, A. Garsuch, T. Weiss, L.F. Nazar, *Nat. Commun.* **2015**, *6*, 5682.
- [26] S. Rehman, S. J. Guo, Y. L. Hou, *Adv. Mater.* **2016**, *28*, 3167.
- [27] B. Campbell, J. Bell, H. H. Bay, Z. Favors, R. Lonescu, C. S. Ozkan, M. Ozkan, *Nanoscale* **2015**, *7*, 7051.
- [28] J. Jiang, J. Zhu, W. Ai, X. Wang, Y. Wang, C. Zou, W. Huang, T. Yu, *Nat. Commun.* **2015**, *6*, 8622v.
- [29] C. Dai, L. Hu, Q. Wang, Y. Chen, J. Han, J. Jiang, Y. Zhang, B. Shen, Y. Niu, S. Bao, M. Xu, *Energy Storage Mater.* **2017**, *8*, 202.
- [30] X. Liang, A. Garsuch, L. F. Nazar, *Angew. Chem. Int. Ed.* **2015**, *54*, 3907.
- [31] Z. W. Seh, J. H. Yu, W. Li, P. C. Hsu, H. Wang, Y. Sun, H. Yao, Q. Zhang, Y. Cui, *Nat. Commun.* **2014**, *5*, 5017.
- [32] H. Xu, A. Manthiram, *Nano Energy* **2017**, *33*, 124.
- [33] Q. Pang, D. Kundu, M. Cuisinier, L.F. Nazar, *Nat. Commun.* **2014**, *5*, 4759.

- [34] Q. Pang, D. Kundu and L. F. Nazar, *Mater. Horiz.* **2016**, *3*, 130.
- [35] Z. Li, J. Zhang, B. Guan, D. Wang, L. M. Liu and X. W. Lou, *Nat. Commun.* **2016**, *7*, 13065.
- [36] H. Al Salem, G. Babu, C. V. Rao and L. M. Arava, *J. Am. Chem. Soc.*, **2015**, *137*, 11542.
- [37] J. Park, B. C. Yu, J. S. Park, J. W. Choi, C. Kim, Y. E. Sung, J. B. Goodenough, *Adv. Energy Mater.* **2017**, 1602567.
- [38] L. Li, L. Chen, S. Mukherjee, J. Gao, H. Sun, Z. Liu, X. Ma, T. Gupta, C.V. Singh, W. Ren, H.-M. Cheng, N. Koratkar, *Adv. Mater.* **2017**, *29*, 1602734.
- [39] R. J. Bouchard, P. A. Russo, A. Wold, *Inorg. Chem.* **1965**, *4*, 685.
- [40] W. Liu, S. W. Lee, D. Lin, F. Shi, S. Wang, A. D. Sendek, Y. Cui, *Nature Energy* **2017**, *2*, 17035.
- [41] L. Yu, H. Hu, H. B. Wu, X. W. Lou, *Adv. Mater.* **2017**, 1604563.
- [42] J. Xiao, L. Wan, S. Yang, F. Xiao and S. Wang, *Nano Lett.* **2014**, *14*, 831.
- [43] L. Zhou, Z. Zhuang, H. Zhao, M. Lin, D. Zhao, L. Mai, *Adv. Mater.* **2017**, 1602914.
- [44] G. Liu, B. Wang, L. Wang, T. Liu, T. Gao, D. Wang, *RSC Adv.* **2016**, *6*, 54076.
- [45] Y. C. Du, X. S. Zhu, X. S. Zhou, L. Y. Hu, Z. H. Dai and J. C. Bao, *J. Mater. Chem. A* **2015**, *3*, 6787.
- [46] T. Chen, L. Ma, B. Cheng, R. Chen, Y. Hu, G. Zhu, Y. Wang, J. Liang, Z. Tie, Z. Jin, *Nano Energy* **2017**, *38*, 239.
- [47] Q. Qu, T. Gao, H. Zheng, Y. Wang, X. Li, X. Li, J. Chen, Y. Han, J. Shao, H. Zheng, *Adv. Mater. Interfaces* **2015**, *2*, 1500048.

- [48] G. Zhou, H. Tian, Y. Jin, X. Tao, B. Liu, R. Zhang, Z.W. Seh, D. Zhuo, Y. Liu, J. Sun, J. Zhao, C. Zu, D.S. Wu, Q. Zhang, Y. Cui, *Proc. Natl. Acad. Sci. USA* **2017**, *114*, 840.
- [49] Y. Peng, B. Li, Y. Wang, X. He, J. Huang, J. Zhao, *ACS Appl. Mater. Interfaces* **2016**, *9*, 4397.
- [50] D. R. Deng, T. H. An, Y. J. Li, Q. H. Wu, M. S. Zheng, Q. F. Dong, *J. Mater. Chem. A* **2016**, *4*, 16184.
- [51] C. Zheng, S. Niu, W. Lv, G. Zhou, J. Li, S. Fan, Y. Deng, Z. Pan, B. Li, F. Kang, Q. H. Yang, *Nano Energy* **2017**, *33*, 306.
- [52] Z. Sun, J. Zhang, L. Yin, G. Hu, R. Fang, H. M. Cheng, F. Li, *Nat. Commun.* **2017**, *8*, 14627.
- [53] G. Kresse, J. Furthmuller, *Comput. Mater. Sci.* **1996**, *6*, 15-50.
- [54] J. P. Perdew, J. A. Chevary, S. H. Vosko, K. A. Jackson, M. R. Pederson, D. J. Singh, C. Fiolhais, *Phys. Rev. B* **1992**, *46*, 6671-6687.
- [55] J. P. Perdew, K. Burke, M. Ernzerhof, *Phys. Rev. Lett.* **1996**, *77*, 3865-3868.
- [56] G. Henkelman, H. Jónsson, *J. Chem. Phys.* **2000**, *113*, 9901-9904.
- [57] G. Henkelman, H. Jónsson, *J. Chem. Phys.* **2000**, *113*, 9978-9985.
- [58] Klimeš J., Bowler D.R., A. Michaelides, *Phys. Rev. B* **2011**, *83*, 195131-195144.

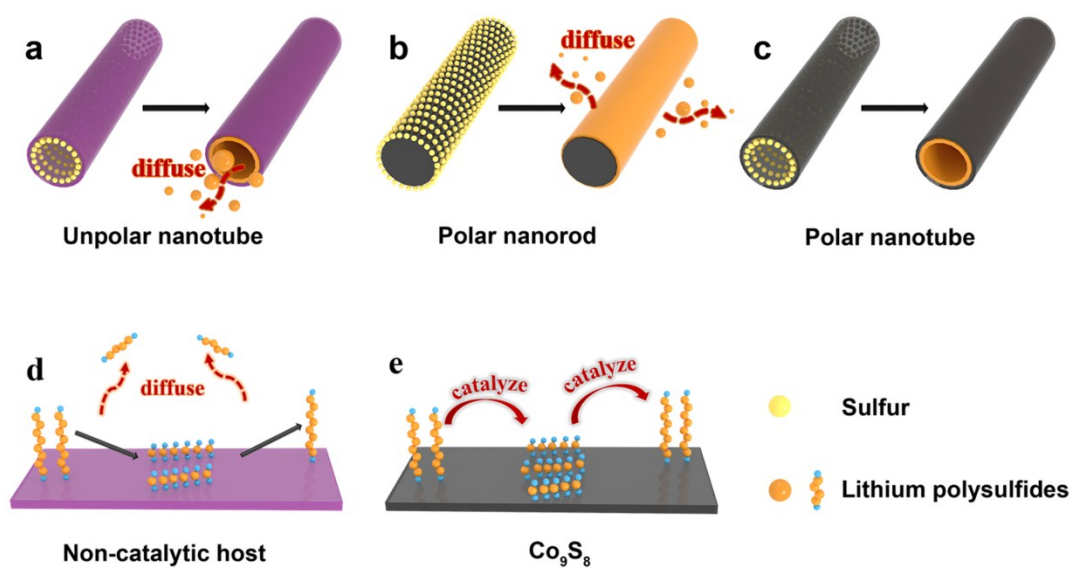


Figure 1 Schematic illustration of the advantages of honeycomb-like spheres constructed from hollow, metallic, and polar Co_9S_8 tubules as sulfur hosts. a) Nonpolar tubular materials are not able to suppress the dissolution of LiPSs due to weak interaction. b) For solid polar materials, LiPSs far away from the polar surface can easily diffuse into the electrolyte. c) For hollow polar tubular structure, it is difficult for the LiPSs to diffuse out from the cathode into the electrolyte due to structural and chemical encapsulation. d) For non-catalytic host, the LiPSs can easily diffuse into the electrolyte because of slow kinetics. e) Catalytic Co_9S_8 accelerates polysulfide conversion and reduces diffusion.

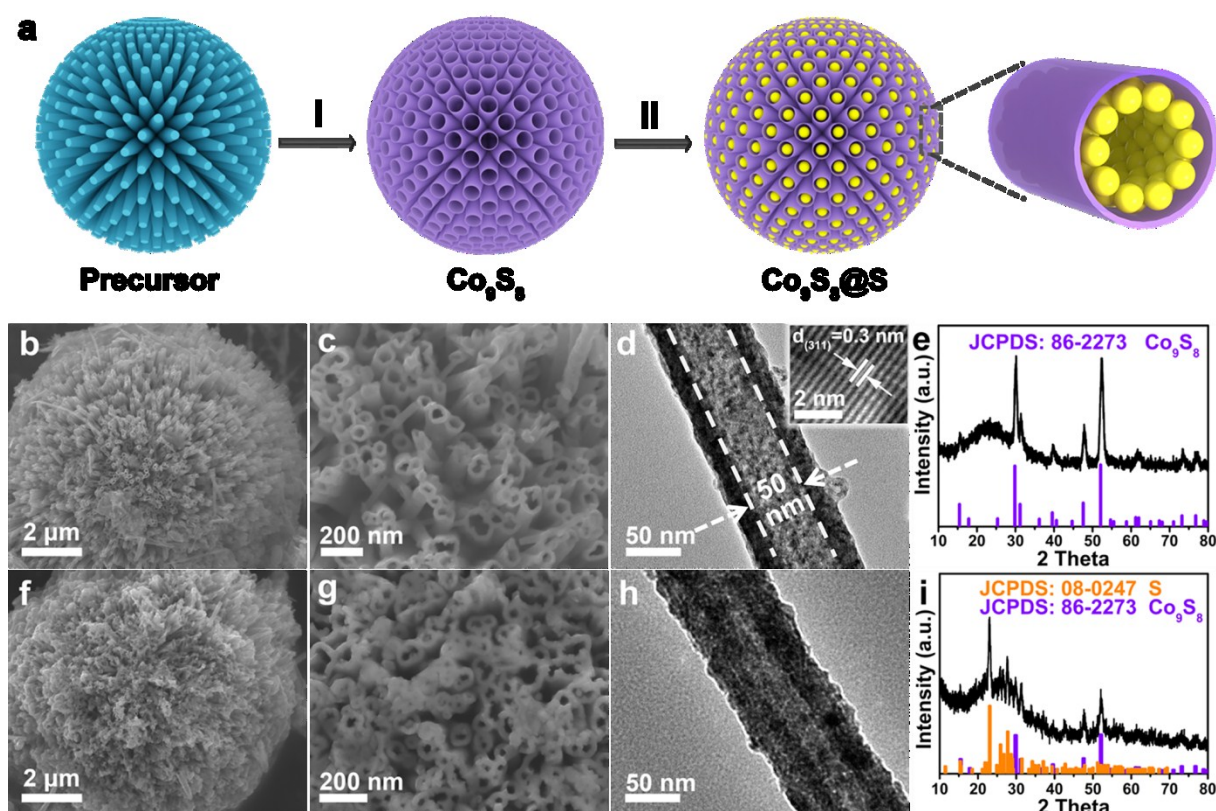


Figure 2 Characterization of Co_9S_8 and $\text{S}@\text{Co}_9\text{S}_8$. a) Schematic illustration of the fabrication of $\text{S}@\text{Co}_9\text{S}_8$ composites. FESEM and TEM images and XRD patterns of b-e) the honeycomb-like Co_9S_8 and f-i) $\text{S}@\text{Co}_9\text{S}_8$ composites.

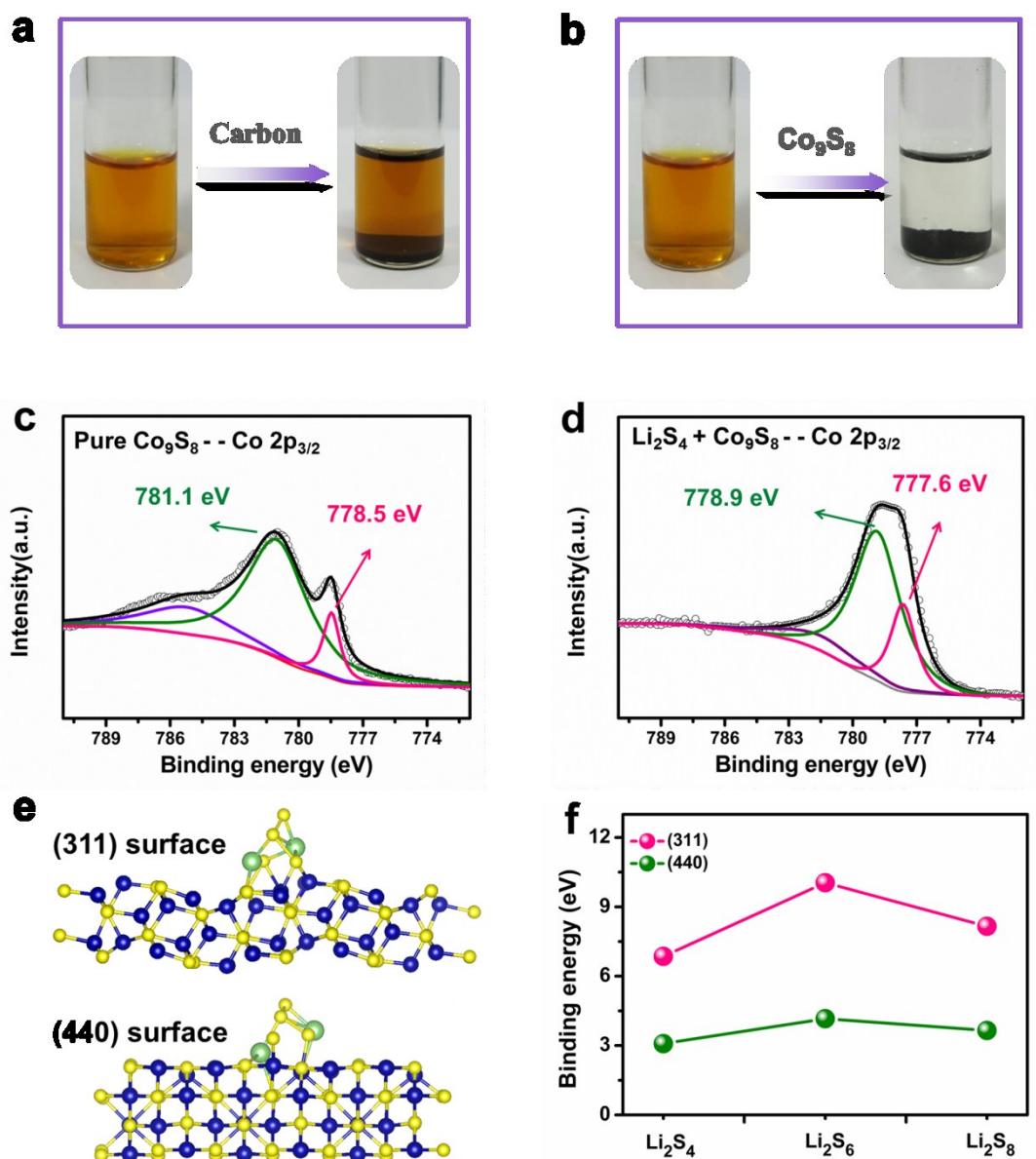


Figure 3 The strong interaction between Co_9S_8 and LiPSs. Polysulfide entrapment by a) carbon and b) Co_9S_8 . High-resolution XPS spectra of Co $2p_{3/2}$ of c) the pure Co_9S_8 and d) $\text{Co}_9\text{S}_8 + \text{Li}_2\text{S}_4$ composite. e) Relaxed Li_2S_4 -adsorbed structures on both (311) (upper) and (440) (lower) surfaces of Co_9S_8 calculated with DFT. Blue atoms are Co, yellow are S, and green are Li. f) Calculated binding energy between LiPSs (Li_2S_4 , Li_2S_6 , and Li_2S_8) and Co_9S_8 surfaces.

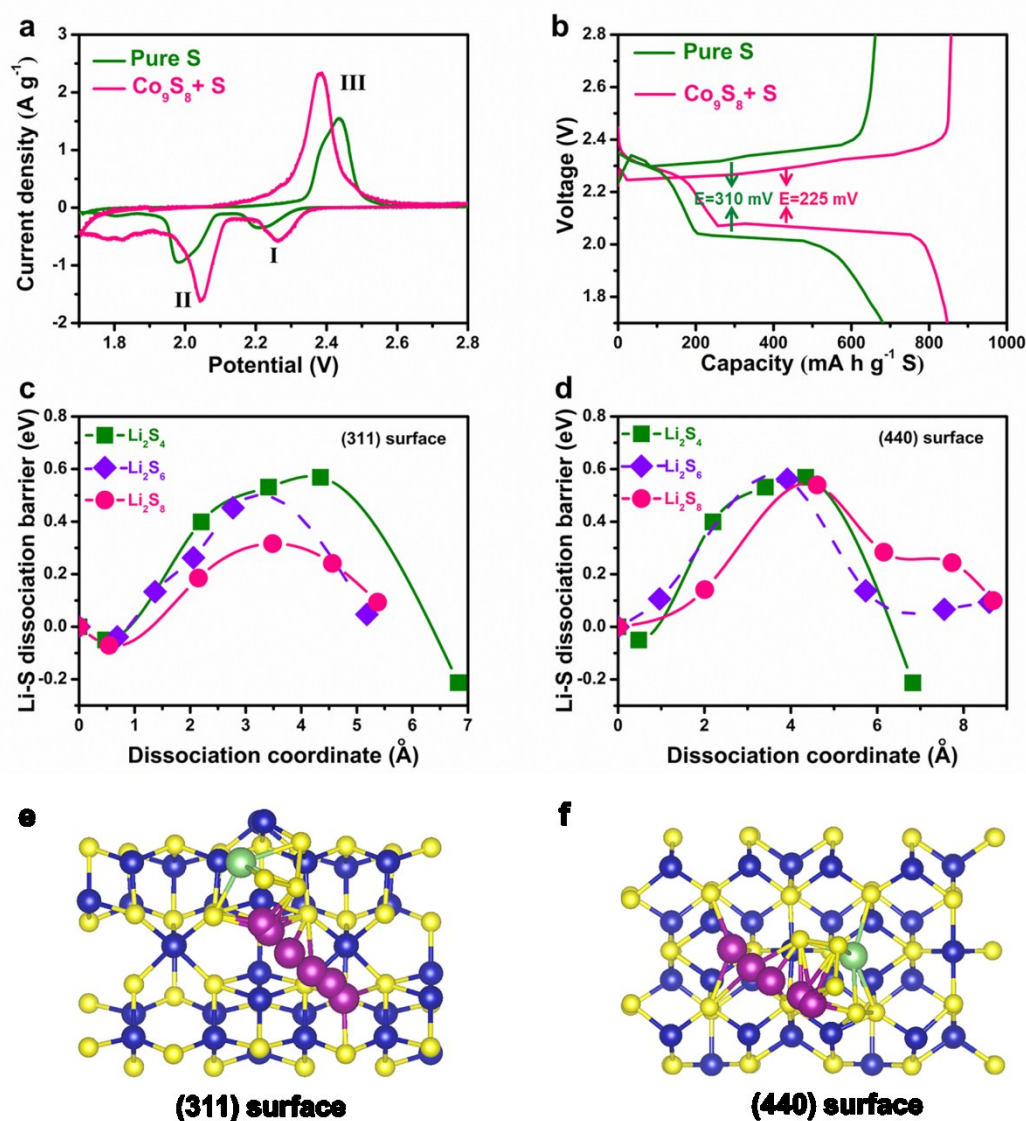


Figure 4 Improved electrochemical reaction kinetics of Co_9S_8 . a) CV curves of S and $\text{Co}_9\text{S}_8 + \text{S}$ electrodes. b) Discharge-charge curves of S and $\text{Co}_9\text{S}_8 + \text{S}$ electrodes. c,d) Dissociation barriers between Li and S in Li_2S_4 , Li_2S_6 , and Li_2S_8 on both the (311) and (440) surfaces. e,f) The decomposition process of Li-S dissociation in relaxed Li_2S_4 -adsorbed structures; purple atoms are migrating Li atoms. Blue atoms are Co, yellow are S, and green are Li.

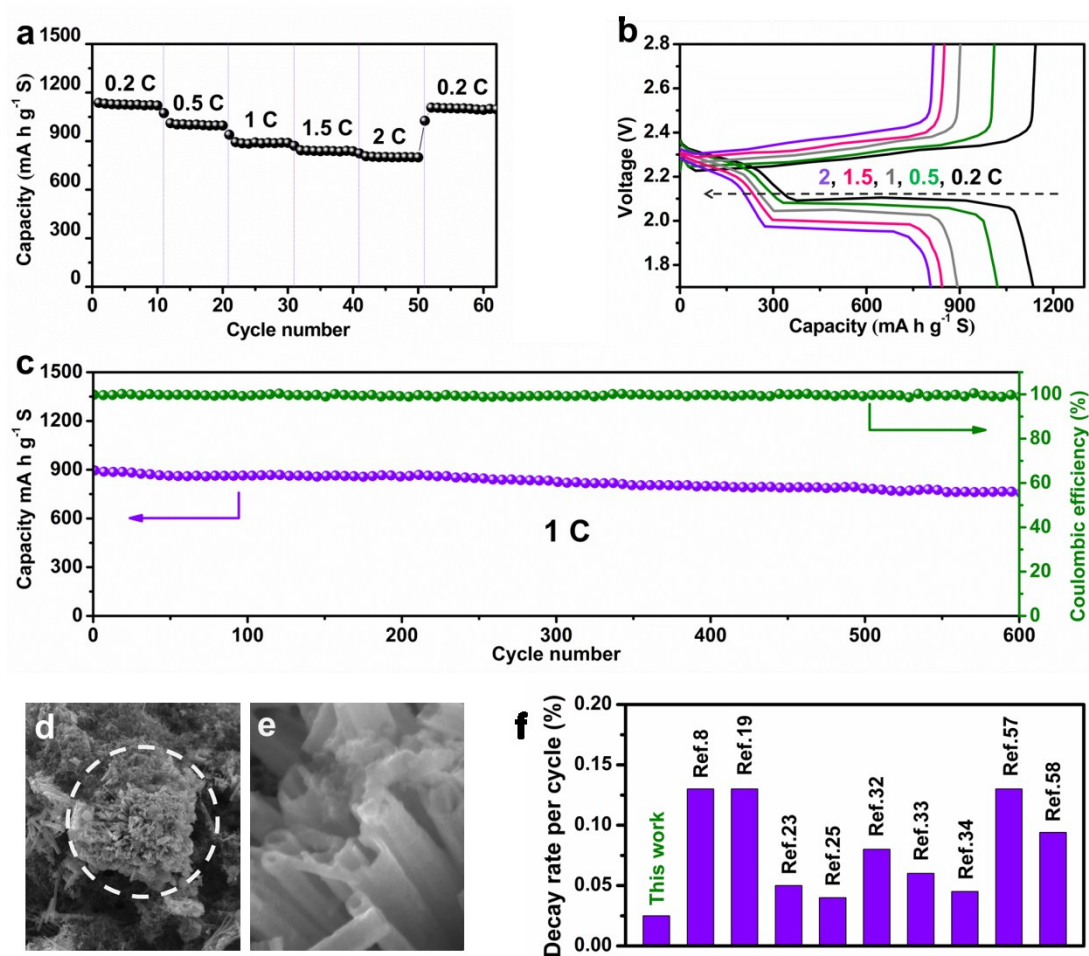


Figure 5 Electrochemical performance of the S@Co₉S₈ nanocomposite. a) Rate capabilities and b) discharge-charge curves at 0.2, 0.5, 1, 1.5 and 2 C. c) Cycling performance at 1 C over 600 cycles. d,e) FESEM images of the S@Co₉S₈ composite after cycling. f) Comparison of the decay rate per cycle with other Li-S cathode materials reported in the literature.

Highly conductive sulfiphilic honeycomb-like spheres constructed from hollow, metallic, and polar Co_9S_8 tubules have been synthesized. Experiment and simulation show that Co_9S_8 is a polysulfide immobilizer and electrocatalyst in Li-S batteries. Benefiting from excellent conductivity, strong LiPSs adsorption capability, and high catalytic activity, the $\text{S@Co}_9\text{S}_8$ composite cathode delivers a stable cycle life with a high discharge capacity for Li-S batteries.

Keyword: hollow Co_9S_8 tubules, honeycomb-like sphere, lithium sulfur batteries, lithium polysulfides, reaction kinetics

Chunlong Dai, Jin-Myoung Lim, Minqiang Wang, Linyu Hu, Yuming Chen,* Zhaoyang Chen, Hao Chen, Shujuan Bao, Bolei Shen, Yi Li, Graeme Henkelman,* Maowen Xu*

Honeycomb-like spherical cathode host constructed from hollow metallic and polar Co_9S_8 tubules for advanced lithium-sulfur batteries

ToC figure

